PERGAMON

International Journal of Heat and Mass Transfer 42 (1999) 4345–4362

International Journal of HEAT and MASS TRANSFER

www.elsevier.com/locate/ijhmt

Effect of wall electrical conductivity and magnetic field orientation on liquid metal flow in a geometry similar to the horizontal Bridgman configuration for crystal growth

R. Bessaih[a,*], M. Kadja[a], Ph. Marty[b]

[a]*Institut de Génie-Mécanique, Université de Constantine, Route d'Ain El. Bey, Constantine, 25000, Algeria*
[b]*Laboratoire des Ecoulements Géophysiques et Industriels, BP. 53 X, 38041, Grenoble Cedex, France*

Received 10 July 1998; received in revised form 2 March 1999

Abstract

The article deals with magnetic field damping of free-convective flows in cavities similar to those used in artificial growth of single crystals from melts (horizontal Bridgman configurations) and having aspect ratios A equal to 1 or 4. The combined effect of wall electrical conductivity and direction of the magnetic field on the buoyancy-induced flow of gallium was investigated numerically. The validation of the numerical method was achieved by comparison with both experimental and analytical data found in the literature. The plotted results for variation of velocity, temperature and Nusselt number in terms of the Hartmann number Ha and Rayleigh number Ra showed a considerable decrease in convection intensity as the magnetic field is increased, especially for values of Ra situated around 10^5. The calculations also showed that the horizontally directed magnetic field (perpendicular to the y–z plane) is the most effective in controlling the flow and hence the speed of growth of the crystal and its composition in dopants. Also, wall electrical conductivity enhances damping by changing the distribution of the induced electric current to one which augments the magnitude of the Lorentz force in regions where it acts as a sink and diminishing it in the remaining parts of the cavity.

1. Introduction

In the majority of the methods used for synthetic production of single crystals, the crystal grows slowly from a fluid nutrient contained in a crucible of variable geometry. The latter is pulled from the hot region of a furnace to a colder one where the system solidifies. The liquid phase is distinguished from the solid phase by the solidification front (Fig. 1). In order to keep the nutrient in its molten state, the crucible must be maintained at a temperature above the freezing point which of course is the temperature at the crystal growth interface (the solidification front). The resulting temperature gradient within the melt generates natural convective flow. These motions are of great concern to the crystal grower because they control the transport of dopant, impurities and heat to the growth interface. This concern is reflected in the numerous review articles on the subject that have been published over the past twenty years (Carruthers [1], Hurle [2], Kobayashi [3], Langlois [4]).

Also, crystal materials are good electrical conductors in their liquid state. This property opened the possibility of using MHD effects to modify the fluid motion and therefore obtain crystals which satisfy better the

* Corresponding author. Tel.: +213-4-923-100; fax: +213-4-941-066.

E-mail address: bessaih@caramail.com (R. Bessaih)

0017-9310/99/$ - see front matter
PII: S0017-9310(99)00097-6

Nomenclature

A	aspect ratio
B	magnetic field [T]
Bo	vertical magnetic field [T] (see Fig. 1)
Fx	Lorentz force in the x-direction
Fy	Lorentz force in the y-direction
Fz	Lorentz force in the z-direction
g	gravitational acceleration [m s^{-2}]
Ha	Hartmann number $= BL(\sigma/\rho\nu)^{1/2}$
jx	electric current in the x-direction [A m^{-2}]
Jx	dimensionless electric current in the x-direction, $= jx/(\alpha/L)\sigma B$
jy	electric current in the y-direction [A m^{-2}]
Jy	dimensionless electric current in the y-direction, $= jy/(\alpha/L)\sigma B$
jz	electric current in the z-direction [A m^{-2}]
Jz	dimensionless electric current in the z-direction, $= jz/(\alpha/L)\sigma B$
L	length of the enclosure [m]
$\overline{Nu}$	average Nusselt number
N_x	nodes number in the x-direction
N_y	nodes number in the y-direction
N_z	nodes number in the z-direction
p	pressure [Pa]
P	dimensionless pressure, $= p/\rho_0(\alpha/L)^2$
Pr	Prandtl number, $= \nu/\alpha$
Ra	Rayleigh number, $= g\beta(T_H - T_C)L^3/(\alpha\nu)$
Re_m	magnetic Reynolds number, $= \mu\sigma\lvert V_0\rvert L$
t	time [s]
T	temperature [K]
T_H	hot temperature [K]
T_C	cold temperature [K]
T_W	wall temperature [K]
u	velocity in the x-direction [m s^{-1}]
U	dimensionless velocity in the x-direction, $= u/(\alpha/L)$
v	velocity in the y-direction [m s^{-1}]
V	dimensionless velocity in the y-direction, $= v/(\alpha/L)$
w	velocity in the z-direction [m s^{-1}]
W	dimensionless velocity in the z-direction, $= w/(\alpha/L)$
x	Cartesian coordinate in the x-direction [m]
X	dimensionless Cartesian coordinate in the x-direction, $= x/L$
y	Cartesian coordinate in the y-direction [m]
Y	dimensionless Cartesian coordinate in the y-direction, $= y/L$
z	Cartesian coordinate in the z-direction [m]
Z	dimensionless Cartesian coordinate in the z-direction, $= z/L$.

Greek symbols

α	thermal diffusivity [m^2 s^{-1}]
β	thermal expansion coefficient [K^{-1}]
δ_H	dimensionless thickness Hartmann layer, $= Ha^{-1}$
δ_S	dimensionless thickness side layer, $= Ha^{-1/2}$
θ	dimensionless temperature, $= (T - T_C)/(T_H - T_C)$
μ_m	magnetic permeability [H m^{-1}]
ν	kinematic viscosity of the fluid [m^2 s^{-1}]
ρ	density of the fluid [kg m^{-3}]
ρ_0	density at reference temperature [kg m^{-3}]
σ	electrical conductivity [Ω^{-1} m^{-1}]
τ	dimensionless time, $= t/(L^2/\alpha)$
ψ	electrical potential [V]
φ	dimensionless electric potential, $= \psi/(\alpha B)$.

requirements of present technology. One can mention for example the significant improvements in the quality of silicon crystals that have been obtained by Czochralski growth in a strong magnetic field (Hoshikawa et al. [5], Kim et al. [6]). The modification of fluid motion consists in the quenching of flow oscillations and therefore the temperature fluctuations of which they are responsible. This improves the resulting crystal quality by avoiding the oscillatory crystal growth which may result from temperature fluctuations and which is characterised by a non-uniform distribution of dopant in the crystal.

More recently, Campbell and Koster [7] experimentally proved that the intensity of convection may modify the shape of the solidification front. This was done using X-rays visualisation of pure gallium in a horizontal Bridgman configuration. The control of convection intensity can be achieved by exposing the flow to a magnetic field of varying or constant strength and/or direction (Davoust et al. [8], Benhadid and Henry [9], Alchaar et al. [10], Bühler [11]).

The work of Davoust et al. [8] is a review of recent results on the MHD damping and reorganisation of the convective flow in a horizontal Bridgman configuration. The numerical results obtained for $0 \leq Ha \leq 100$ complement their asymptotic theory

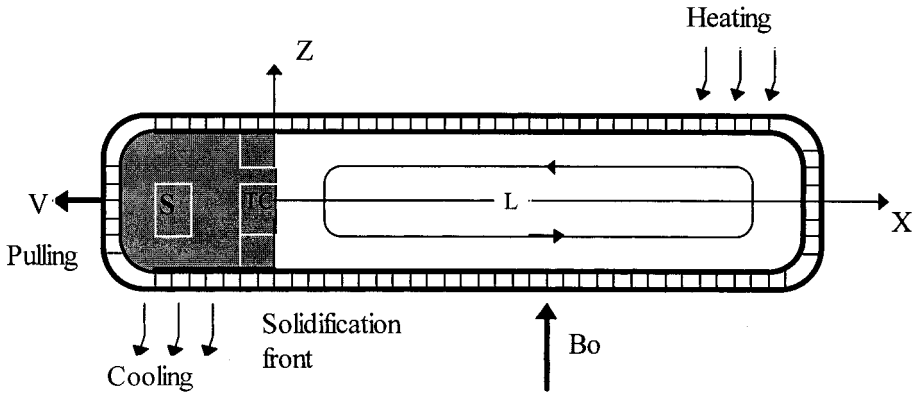

Fig. 1. Horizontal Bridgman crystal growth configuration.

and show how the typical MHD flow organisation with cores, Hartmann layers and side layers builds up as *Ha* increases. An experiment, using mercury to model the liquid pool, allowed the authors to check their predictions.

Alchaar et al. [10] numerically investigated the effect of a transverse magnetic field on buoyancy driven convection in a shallow rectangular cavity. The study covers the range of the Rayleigh number, *Ra*, from 10^2 to 10^5, the Hartmann number *Ha*, from 0 to 10^2, the Prandtl number, *Pr* from 0.005 to 1 and aspect ratio of cavity, A from 1 to 6. Comparison of their results was made with an existing analytical solution (Garandet et al. [12]). At high Hartmann numbers, both analytical and numerical analyses revealed that the velocity gradient in the core is constant outside the two Hartmann layers at the vicinity of the walls normal to the magnetic field.

The numerical work by Benhadid and Henry focused on the action of a constant magnetic field on the flow that develops in a differentially heated Bridgman cylindrical cavity. Their three-dimensional flow results showed that the strength of the applied magnetic field leads to several fundamental changes in the properties of thermal buoyant convection. The convective circulation progressively looses its intensity and is reorganised specifically depending on the direction (vertical, longitudinal or transversal) of the applied magnetic field. This leads to the appearance of specific velocity profiles, of Hartmann layers and of parallel layers, and to the tendency towards two-dimensionality. The authors linked these structural changes with the repartition of the induced electric current inside the cavity.

Bühler investigated analytically buoyancy driven laminar MHD flow in long vertical channels. He derived solutions for general temperature distributions. He found the typical subregions for the flow namely the inviscid core, surrounded by Hartmann layers and side layers. He obtained high velocity jets along perfectly conducting walls and concluded that the main difference compared with pressure driven duct flows is that the core not necessarily exhibits a two-dimensional behaviour.

The present contribution falls within the scope of the latter two works but deals for simplicity with a cubic enclosure filled with gallium. The combined effects on the flow structure of wall electrical conductivity and magnetic field orientation are numerically investigated and the results are discussed within the context of Bridgman crystal growth.

2. The mathematical model

2.1. The model equations

The configuration chosen is the cubical enclosure shown in Fig. 2. One vertical wall is maintained at a high temperature T_H (which corresponds to the temperature of the furnace in a real crystal growth situation) and the opposing vertical wall is maintained at a lower temperature T_C (which corresponds to the temperature at the solidification front (Fig. 1)). The remaining walls are thermally insulated. The enclosure is filled with liquid gallium whose Prandtl number is 0.025. The flow can be exposed to a uniform magnetic field parallel to one of the three coordinate directions. In order to evaluate the effect of applying the magnetic field on the natural convection of the liquid metal, the governing equations are obtained using the following assumptions:

- Joule heating is negligible.
- Viscous dissipation is negligible.
- The induced magnetic field is negligible because $Re_m \ll 1$.

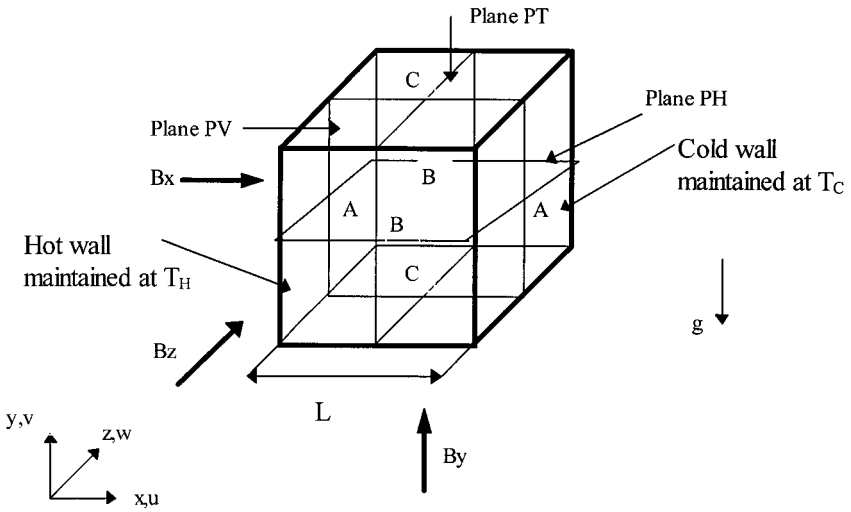

Fig. 2. Various orientations of the applied magnetic field in a metal filled enclosure.

- The liquid metal is not magnetized ($\mu_m = 1$).
- The liquid metal is incompressible and Newtonian.
- The Boussinesq approximation holds.

The adimensionnalised equations are given below [Eqs. (1)–(6)]. The quantities used for adimensionnalising the coordinates, time, velocities, pressures, temperature and current density are, respectively, defined by the formulae:

$$X,Y,Z = x,y,z/L; \quad \tau = t/(L^2/\alpha);$$

$$U,V,W = u,v,w/(\alpha/L); \quad P = p/\rho_0(\alpha/L)^2;$$

$$\theta = (T - T_C)/(T_H - T_C); \quad J = j/(\alpha/L)\sigma B$$

where α, ρ, σ, t, j, B represent, respectively, the thermal diffusivity of the metal, its density, its electrical conductivity, time, electric current intensity and magnetic field intensity. u, v and w are the velocity components in directions x, y and z, respectively.

Continuity

$$\frac{\partial U}{\partial X} + \frac{\partial V}{\partial Y} + \frac{\partial W}{\partial Z} = 0 \tag{1}$$

x-direction momentum

$$\frac{\partial U}{\partial \tau} + \frac{\partial (UU)}{\partial X} + \frac{\partial (VU)}{\partial Y} + \frac{\partial (WU)}{\partial Z}$$

$$= -\frac{\partial P}{\partial X} + Pr\left\{\frac{\partial^2 U}{\partial X^2} + \frac{\partial^2 U}{\partial Y^2} + \frac{\partial^2 U}{\partial Z^2}\right\} + Fx \tag{2}$$

y-direction momentum

$$\frac{\partial V}{\partial \tau} + \frac{\partial (UV)}{\partial X} + \frac{\partial (VV)}{\partial Y} + \frac{\partial (WV)}{\partial Z}$$

$$= -\frac{\partial P}{\partial Y} + Pr\left\{\frac{\partial^2 V}{\partial X^2} + \frac{\partial^2 V}{\partial Y^2} + \frac{\partial^2 V}{\partial Z^2}\right\} + Ra\,Pr$$

$$\theta + Fy \tag{3}$$

z-direction momentum

$$\frac{\partial W}{\partial \tau} + \frac{\partial (UW)}{\partial X} + \frac{\partial (VW)}{\partial Y} + \frac{\partial (WW)}{\partial Z}$$

$$= -\frac{\partial P}{\partial Z} + Pr\left\{\frac{\partial^2 W}{\partial X^2} + \frac{\partial^2 W}{\partial Y^2} + \frac{\partial^2 W}{\partial Z^2}\right\} + Fz \tag{4}$$

Energy

$$\frac{\partial \theta}{\partial \tau} + \frac{\partial (U\theta)}{\partial X} + \frac{\partial (V\theta)}{\partial Y} + \frac{\partial (W\theta)}{\partial Z}$$

$$= \frac{\partial^2 \theta}{\partial X^2} + \frac{\partial^2 \theta}{\partial Y^2} + \frac{\partial^2 \theta}{\partial Z^2} \tag{5}$$

Electric potential

$$\frac{\partial^2 \varphi}{\partial X^2} + \frac{\partial^2 \varphi}{\partial Y^2} + \frac{\partial^2 \varphi}{\partial Z^2} = \frac{\partial W}{\partial Y} - \frac{\partial V}{\partial Z} \tag{6a}$$

(horizontally applied magnetic field)

$$\frac{\partial^2 \varphi}{\partial X^2} + \frac{\partial^2 \varphi}{\partial Y^2} + \frac{\partial^2 \varphi}{\partial Z^2} = \frac{\partial U}{\partial Z} - \frac{\partial W}{\partial X} \tag{6b}$$

(vertically applied magnetic field)

$$\frac{\partial^2\varphi}{\partial X^2}+\frac{\partial^2\varphi}{\partial Y^2}+\frac{\partial^2\varphi}{\partial Z^2}=\frac{\partial V}{\partial X}-\frac{\partial U}{\partial Y} \tag{6c}$$

(transversally applied magnetic field)

where:

$$Ra=\frac{g\beta(T_H-T_C)L^3}{\alpha\nu} \quad \text{and} \quad Pr=\frac{\nu}{\alpha}$$

are the Rayleigh and Prandtl numbers, respectively. The above equations have been obtained after taking the divergence of Ohm's law i.e.

$$\mathbf{J}=\sigma(-\nabla\varphi+\mathbf{V}\times\mathbf{B})$$

and introducing the conservation of charge principle:

$$\nabla\cdot\mathbf{J}=0$$

Fx, Fy, Fz represent the components of Lorentz force. *Jx, Jy, Jz* represent the electric current in directions *x, y* and *z*. The components of *F* and *J* have different expressions according to the orientation of the magnetic field *B*. The components of *J* have been obtained using Ohm's law whereas those of *F* have been obtained using the equation: $\mathbf{F}=\mathbf{J}\times\mathbf{B}$.

- Case of a horizontal magnetic field

When *B* is applied in the *x*-direction, the expressions are:

$$Fx=0 \quad Jx=-\frac{\partial\varphi}{\partial X}$$

$$Fy=\left(-\frac{\partial\varphi}{\partial Z}-V\right)Ha^2\,Pr \quad Jy=-\frac{\partial\varphi}{\partial Y}+W$$

$$Fz=\left(\frac{\partial\varphi}{\partial Y}-W\right)Ha^2\,Pr \quad Jz=-\frac{\partial\varphi}{\partial Z}-V \tag{7}$$

- Case of a vertical magnetic field

When *B* is applied in the *y*-direction, the expressions are:

$$Fx=\left(\frac{\partial\varphi}{\partial Z}-U\right)Ha^2\,Pr \quad Jx=-\frac{\partial\varphi}{\partial X}-W$$

$$Fy=0 \quad Jy=-\frac{\partial\varphi}{\partial Y}$$

$$Fz=\left(-\frac{\partial\varphi}{\partial X}-W\right)Ha^2\,Pr \quad Jz=-\frac{\partial\varphi}{\partial Z}+U \tag{8}$$

- Case of a transversal magnetic field

When *B* is applied in the *z*-direction, the expressions are:

$$Fx=\left(-\frac{\partial\varphi}{\partial Y}-U\right)Ha^2\,Pr \quad Jx=-\frac{\partial\varphi}{\partial X}+V$$

$$Fy=\left(\frac{\partial\varphi}{\partial X}-V\right)Ha^2\,Pr \quad Jy=-\frac{\partial\varphi}{\partial Y}-U$$

$$Fz=0 \quad Jz=-\frac{\partial\varphi}{\partial Z} \tag{9}$$

where *Ha* is the Hartmann number, $Ha=BL(\sigma/\rho\nu)^{1/2}$.

2.2. Initial and boundary conditions

The above equations have been solved subject to the following conditions:

Initial conditions: at $\tau=0$, $U=V=W=0$ and $\theta=0$.

Boundary conditions: for $\tau>0$

At $x=0$ $\quad U=V=W=0$ (no slip condition) and

$\theta=1$ (fixed wall temperature $T_W=T_H$)

At $X=1$ $\quad U=V=W=0$ and $\theta=0$

(fixed wall temperature $T_W=T_C$)

At $Y=0$ $\quad U=V=W=0$ and $\partial\theta/\partial Y=0$

(thermally insulated wall)

At $Y=1$ $\quad U=V=W=0$ and $\partial\theta/\partial Y=0$

At $Z=0$ $\quad U=V=W=0$ and $\partial\theta/\partial Z=0$

(thermally insulated wall)

At $Z=1$ $\quad U=V=W=0$ and $\partial\theta/\partial Z=0$

- For perfectly electrically insulating walls, the boundary condition for all walls is $(\partial\varphi/\partial n)=0$, where φ represents the electrical potential, and *n* the direction normal to the wall in question.
- For perfectly electrically conducting walls, $\varphi=0$ holds for all walls.

3. The numerical procedure

Eqs. (1)–(6) have been solved by using a finite volume method coupled to a pressure correction equation based on the SIMPLER algorithm (Patankar [13]). Scalar quantities (*P*, θ, and φ) are stored in the

centre of these volumes whereas the vectorial quantities (U, V, W, and J) are stored on the faces. A fully implicit time marching scheme is employed (i.e. solutions have been obtained by marching in time). To discretise the temporal term, a first-order regressive finite difference formula was used. The discretisation of spatial terms required a second-order central difference scheme in the diffusion part of the equations and a power law scheme (Patankar [13]) for the convection part. The discretised equations were solved iteratively in each direction along the axes using the line-by-line Tridiagonal-Matrix-Algorithm.

In MHD-flows boundary layers different to those in ordinary hydrodynamics occur. At walls perpendicular to the magnetic field Hartmann layers of thickness $\delta_H \sim Ha^{-1}$ appear which are characterised by an exponential decay of the velocity towards the wall. At walls parallel to the magnetic field, the so-called side layer exists, which is different in shape and thickness ($\delta_S \sim Ha^{-1/2}$) compared to the Hartmann layers.

In order to capture the Hartmann and side layers and by taking into account the fact that their thickness diminish as Ha increases ($\delta_H \sim Ha^{-1}$ and $\delta_S \sim Ha^{-1/2}$) the grid line densities have been chosen according to the value of the magnetic field B and its direction. These are given in Table 1.

The increments ΔX, ΔY and ΔZ of the grid used are not regular. They were chosen according to geometric progressions of ratio 1.07 which permitted grid refinement near the walls; i.e. in the Hartmann and side layers where large velocity and temperature gradients exist, thus requiring a larger number of nodes (more than five nodes in each layer) in order to resolve the specific characteristics of the MHD flow.

Table 1
Meshes used in the computations

	Ha	Mesh size, $N_x \times N_y \times N_z$
No magnetic field	0	$30 \times 30 \times 20$
x-Direction magnetic field	25	$44 \times 30 \times 20$
	50	$64 \times 30 \times 20$
	75	$70 \times 30 \times 20$
	100	$90 \times 30 \times 20$
y-Direction magnetic field	25	$30 \times 44 \times 20$
	50	$30 \times 64 \times 20$
	75	$30 \times 70 \times 20$
	100	$30 \times 90 \times 20$
z-Direction magnetic field	25	$30 \times 20 \times 44$
	50	$30 \times 20 \times 64$
	75	$30 \times 20 \times 70$
	100	$30 \times 20 \times 90$

The grid used for $Ha = 0$ was chosen after performing grid independency tests. The computed average Nusselt numbers for grids finer than $30 \times 30 \times 20$ only differ by 5×10^{-4} hence the choice of this grid. Convergence of the numerical solution was obtained when the mass, momentum and energy residuals are below 10^{-6}.

4. Results and discussions

4.1. Code validation in the absence of a magnetic field

In the absence of a magnetic field, the momentum Eqs. (2)–(4) are solved after setting $Fx = Fy = Fz = 0$. The results are represented graphically in Figs. 3(a)–(e).

The flow structure is shown by the velocity vectors (Fig. 3(a)) and the velocity profiles along the lines AA and CC (Figs. 3(a) and (b)). Fig. 3(a) shows that at the bottom of the cavity the flow is mainly longitudinal and is directed towards the hot wall (situated at $X = 0.0$) and at the top of the cavity the flow is directed towards the cold wall situated at $X = 1$. These boundary layers extend from the walls to the centre of the cavity, a behaviour which is not common in ordinary fluids (De Vahl Davis [14]). From Figs. 3(a) and (b) one can notice that the U, V, and W profiles are linear throughout the core region extending from $X = 0.25$ to $X = 0.75$, from $Y = 0.25$ to $Y = 0.75$ and from $Z = 0.25$ to $Z = 0.75$. Comparison of Figs. 3(a) and (b) reveals the expected behaviour that the flow in the vertical direction is fastest because of the buoyancy-induced acceleration experienced by fluid particles transported in this direction.

A preliminary validation of the numerical method can be done, at this stage, via theoretical estimation of the magnitude of the maximum velocity, which is approximately 30 (Figs. 3(b) and (c)). One can, in effect, write, for large values of the Rayleigh number, that equilibrium exists between buoyancy forces and inertia forces, which gives:

$$\frac{\rho U^2}{L} \approx \rho g \beta \Delta T$$

where L is a characteristic length. By using the above adimensionalisation, one gets:

$$U = (Ra\,Pr)^{1/2} = (10^5 \times 0.025)^{1/2} \approx 50$$

which is very near to the value in Fig. 3(b). This procedure also allows the estimation of the Peclet number ($Pe = UL/\alpha$) which is therefore given by:

$$Pe = (Ra\,Pr)^{1/2}$$

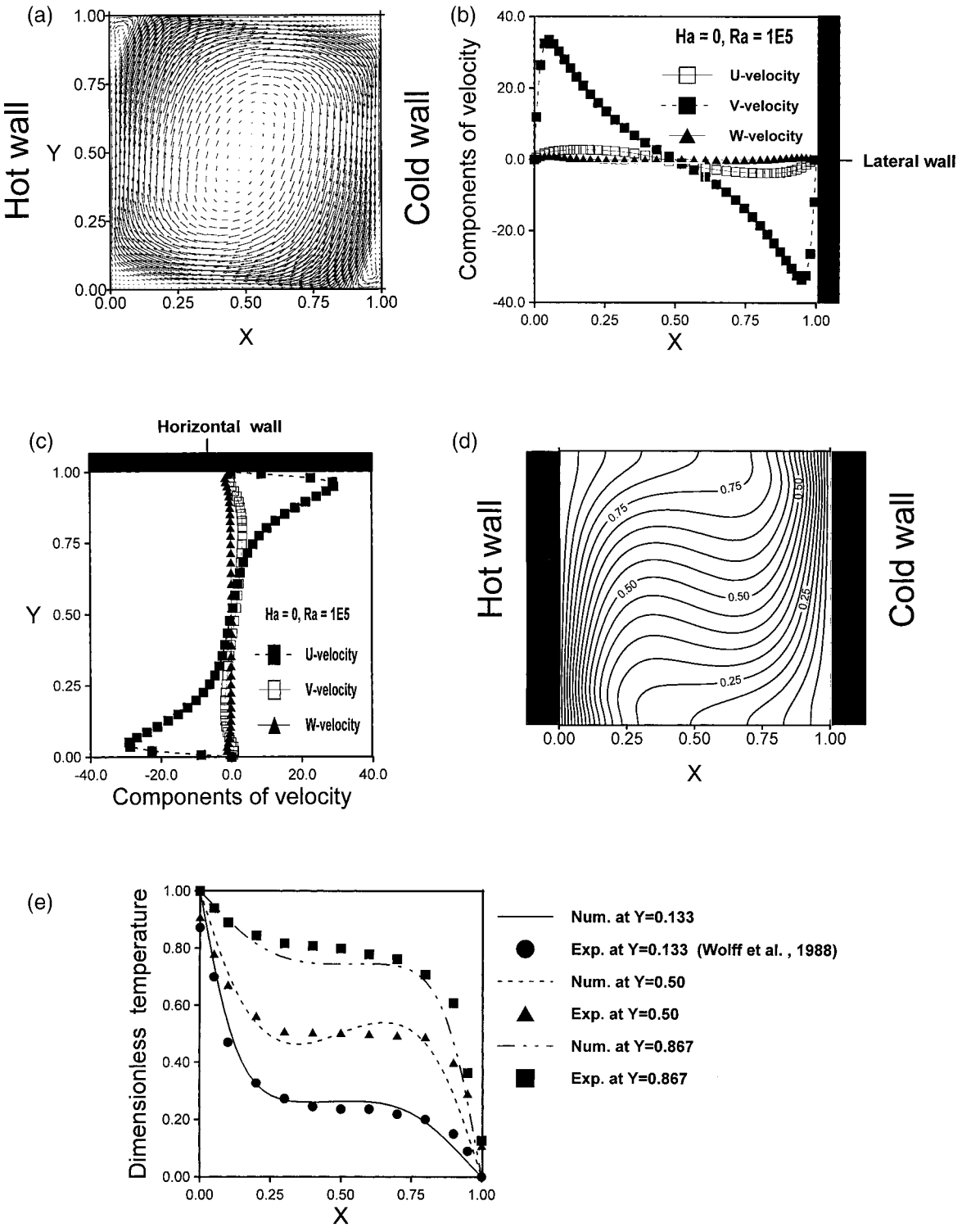

Fig. 3. (a) Velocity vector plot in plane PV for $Ha = 0$ and $Ra = 10^5$. (b) Distribution of velocities along line AA for $Ha = 0$ and $Ra = 10^5$. (c) Distribution of velocities along line CC for $Ha = 0$ and $Ra = 10^5$. (d) Isotherms in plane PV for $Ha = 0$ and $Ra = 10^5$. (e) Temperature distributions for various positions in plane PV, for $Ra = 1.682 \times 10^5$: comparison with experimental data (Wolff et al. [15]).

and has a value of 50. This explains the noticed distortion of the isotherms shown in Fig. 3(d).

The thermal structure of the flow is illustrated by the isotherms of Fig. 3(d) in plane PV, and the three profiles in Fig. 3(e). Fig. 3(e) clearly shows the formation of thermal boundary layers along the vertical walls. Here also the temperature profiles in the core region extending from $X = 0.25$ to $X = 0.75$ are linear. As can be noticed from Fig. 3(d) plotted using a temperature increment $\Delta\theta = 0.05$ between two consecutive isotherms, the isotherms are denser on the lower part of the hot vertical wall and on the top part of the cold vertical wall. This indicates the presence of intense heat transfer across these parts of the walls. In the core region the flow is stably stratified with temperatures increasing from bottom to top. Fig. 3(e) also shows a satisfactory agreement between the predicted and measured temperatures in gallium. However, the numerical results at $Y = 0.50$ show lower values (up to 10% difference) than the experimental data published by Wolff et al. [15], indicating the presence of stronger natural convection. This discrepancy is due to the presence of thermocouple rakes, which tend to suppress the flow; as indicated by Wolff et al.

Code verification was also done using the benchmark solution computed by De Vahl Davis and Jones [16] for natural convection in a square cavity. They present tabulated results for a range of Rayleigh numbers, $Ra = 10^3$, 10^4, 10^5 and 10^6. The quantities U_{max}, V_{max}, Nu_{min}, Nu_{max} and $\overline{Nu}$ of our steady state results are compared with those obtained by their method. The results are presented in Tables 2–5. The quantities

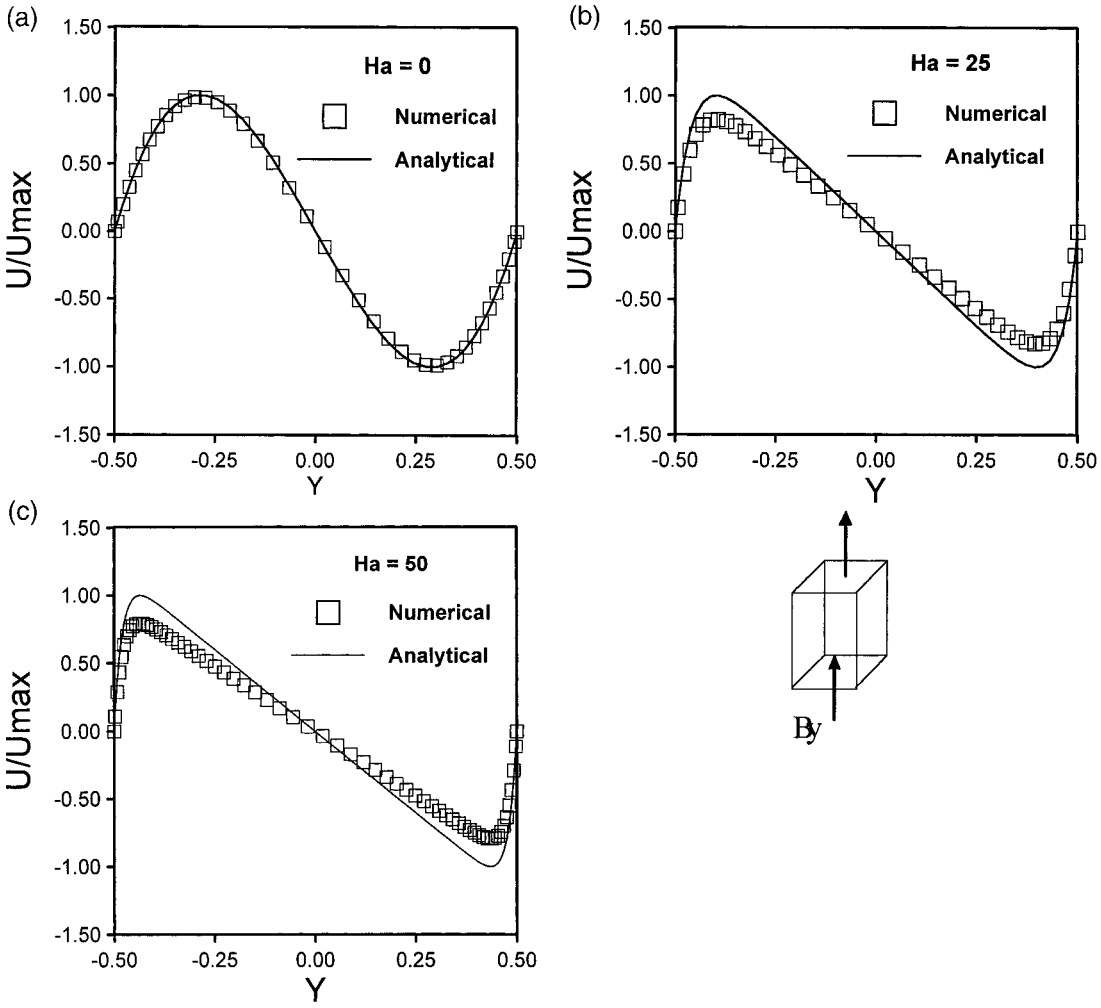

Fig. 4. Velocity distributions in the midplane of the cavity: comparison with analytical results for $Ra = 800$ at the position $X = 2$: (a) $Ha = 0$; (b) $Ha = 25$; (c) $Ha = 50$.

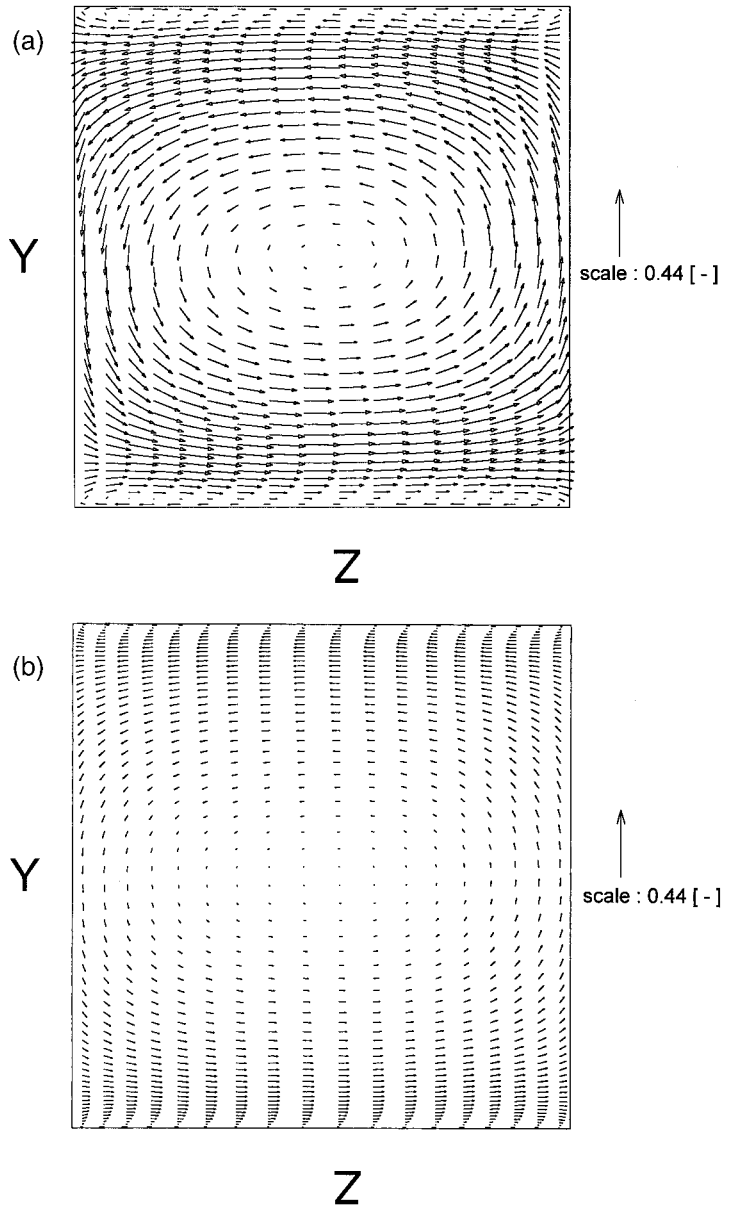

Fig. 5. (a) Current path for $Ha = 25$ in plane PT. (b) Current path for $Ha = 50$ in plane PT.

Table 2
Steady state results for $Ra = 10^3$

$Ra = 10^3$	Present work	Benchmark solution
U_{max}	3.645	3.649
V_{max}	3.700	3.697
Nu_{min}	0.691	0.692
Nu_{max}	1.508	1.505
$\overline{Nu}$	1.118	1.118

Table 3
Steady state results for $Ra = 10^4$

$Ra = 10^4$	Present work	Benchmark solution
U_{max}	16.141	16.178
V_{max}	19.578	19.617
Nu_{min}	0.588	0.586
Nu_{max}	3.548	3.528
$\overline{Nu}$	2.247	2.243

Table 4
Steady state results for $Ra = 10^5$

$Ra = 10^5$	Present work	Benchmark solution
U_{max}	34.982	34.73
V_{max}	68.775	68.59
Nu_{min}	0.751	0.729
Nu_{max}	7.830	7.717
$\overline{Nu}$	4.540	4.519

Table 5
Steady state results for $Ra = 10^6$

$Ra = 10^6$	Present work	Benchmark solution
U_{max}	65.676	64.63
V_{max}	222.598	219.36
Nu_{min}	1.083	0.989
Nu_{max}	18.74	17.925
$\overline{Nu}$	8.945	8.800

U_{max} and V_{max} are obtained from the velocity profiles on the vertical mid-plane and on the horizontal mid-plane, respectively. The average Nusselt number is defined as: $\overline{Nu} = \int_0^1 (\partial\theta/\partial X)\mathrm{d}Y|_{x=0}$. The values of Nu_{max} and Nu_{min} are found along the hot wall. The calculated quantities show a reasonable agreement with the benchmark solution for $Ra = 10^3$, 10^4 and 10^5; however, discretisation errors cause noticeable differences (less than 5%) for $Ra = 10^6$ because at this value of Rayleigh number velocity gradients in the convective terms become important, thus requiring more nodes in order to get a good resolution of the flow.

4.2. Code validation in the presence of a magnetic field

Comparison was first made here with the analytical results obtained by Garandet et al. [12] who studied the effect of a vertical magnetic field on buoyancy driven convection in a two-dimensional shallow cavity (i.e. having an aspect ratio A equal to infinity). Using the parallel flow hypothesis, the authors showed that the velocity distribution in the core region of the cavity follows the law:

$$U = \frac{Ra}{Ha^2}[F\ \sin(Ha\ Y^*) - Y^*] \tag{10}$$

where Y^* is the vertical coordinate starting from the centre of the cavity, and $F = 1/[2\ \sinh(Ha/2)]$.

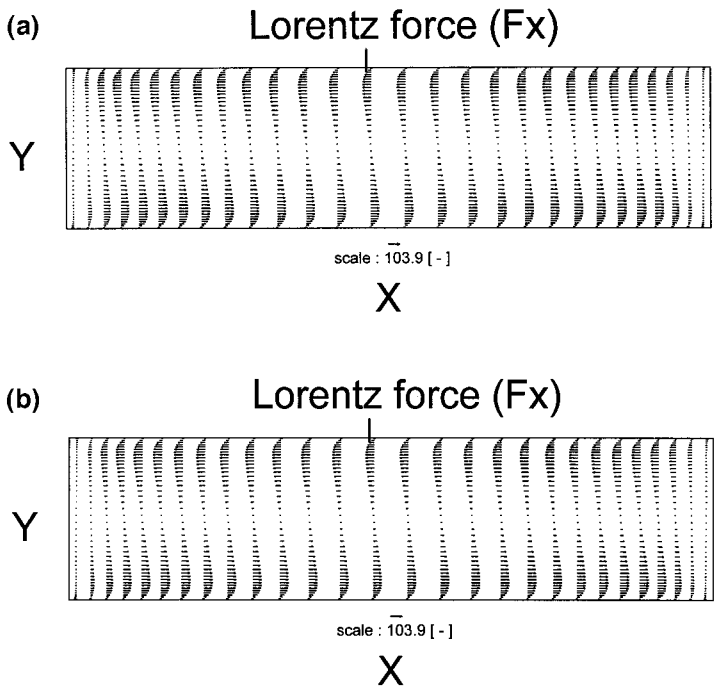

Fig. 6. (a) Component Fx of the Lorentz force for $Ra = 800$ and $Ha = 25$ in plane PV. (b) Component Fx of the Lorentz force for $Ra = 800$ and $Ha = 50$ in plane PV.

Recently Alchaar et al. [10] studied the range of validity of Eq. (10). A good agreement between their numerical results and the results calculated from Eq. (10) is obtained provided that the aspect ratio of the cavity is greater than approximately three. This condition was taken into consideration in the present study and validation of the code was achieved using a cavity of aspect ratio $A = 4$ and of dimensions $4 \times 1 \times 1$. The numerical results obtained for $Ra = 800$ and three values of the Hartmann numbers are compared with their analytical counterparts in Figs. 4(a)–(c). A satisfactory concordance is achieved especially at low values of Ha.

For all values of the Hartmann number, the figures show a velocity which increases from zero at the wall to a peak situated in the viscous sublayer and then drops back to zero at the centre of the cavity (corresponding to $Y = 0$). The profile is cubic when $Ha = 0$.

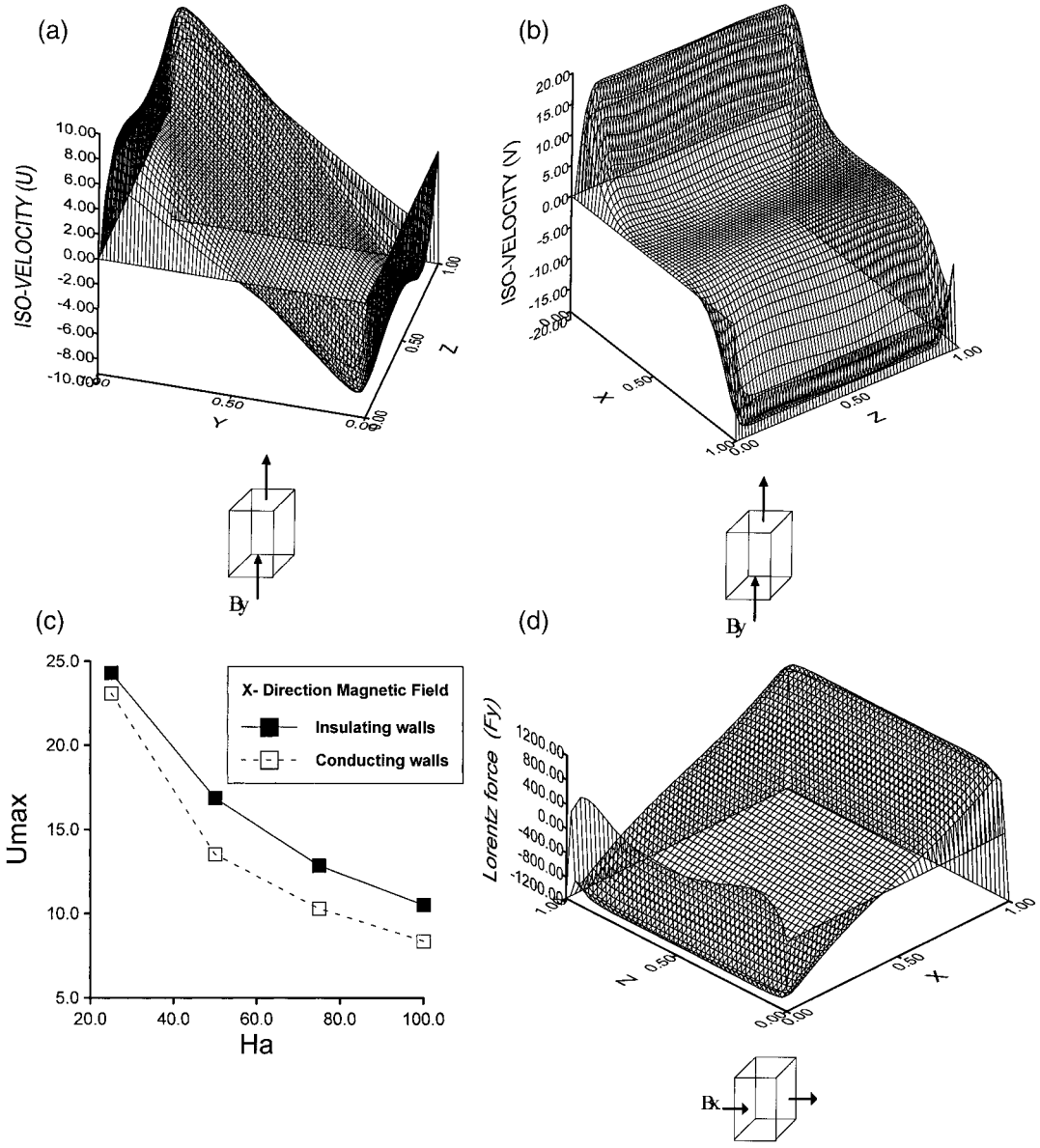

Fig. 7. (a) U-velocity component distribution in plane PT, $Ra = 10^5$, electrically insulating walls. (b) V-velocity component distribution in plane PH, $Ra = 10^5$, electrically insulating walls. (c) Variation of U_{max} with Ha for the x-oriented magnetic field, $Ra = 10^5$ for both insulating and conducting walls. (d) Lorentz force component distribution in plane PH, $Ra = 10^5$, electrically insulating walls. (e) Current path in plane PH for x-directed field, $Ra = 10^5$, electrically insulating walls.

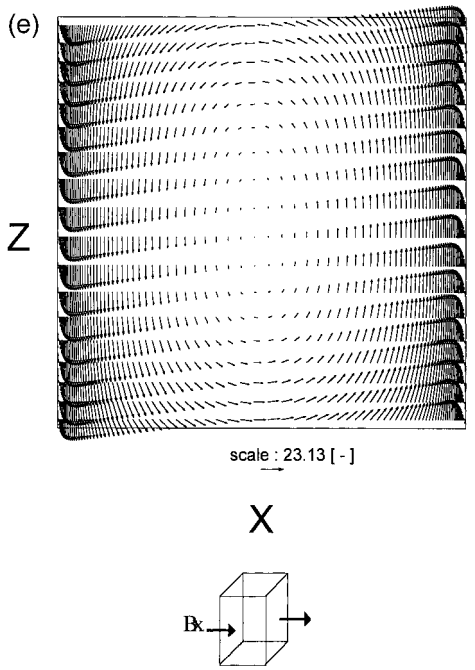

Fig. 7 (*continued*)

When *Ha* is increased, the velocity profile in the core tends to a linear profile. The effect of viscosity cannot, however, be neglected in the vicinity of the walls where one can notice the presence of two thin Hartmann layers.

In order to give a better insight into the physics behind the change in flow pattern, sketches of the current path in plane PT corresponding to $Ha = 25$ and $Ha = 50$ are given, respectively, in Figs. 5(a) and (b). The Lorentz forces produced by the interaction between these currents and the applied vertical field are given, respectively, in Figs. 6(a) and (b). As can be noticed from Figs. 5, the flowing fluid, generates under the action of the magnetic field, currents which are positive in the neighbourhood of the top wall and negative in the neighbourhood of the bottom wall. This difference in sign is due to the different directions of the fluid in contact with the top and bottom walls. Because of this difference in sign, the Lorentz force acting on the top layers of the fluid is negative (i.e. a retarding force) and that acting on the bottom layers positive (i.e. also a retarding force since the fluid flows in the negative direction towards the plane $X = 0$). When the value of *Ha* is increased, the magnitude of Lorentz forces increases (Fig. 6) and therefore reduces the magnitude of the velocity. This provokes the damping of the flow.

A second validation of the present code was performed using the benchmark solution in the work of

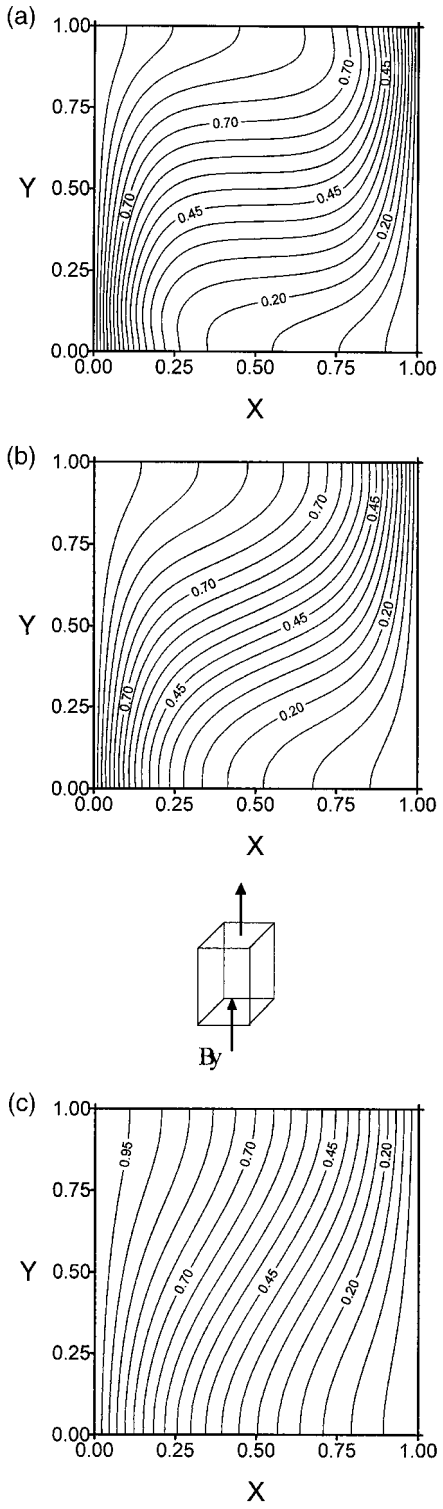

Fig. 8. Isotherms in plane PV for the vertically oriented magnetic field and $Ra = 10^5$: (a) $Ha = 25$; (b) $Ha = 50$; (c) $Ha = 100$.

Table 6
Average Nusselt numbers for $Ra = 10^6$ and $Pr = 0.054$. The magnetic field is oriented in the x-direction

	Present work $\overline{Nu}$ for B_x	Ozoe and Okada $\overline{Nu}$ for B_x
$Ha = 100$	4.4219	4.4577
$Ha = 200$	2.8804	2.9168

Ozoe and Okada [17] who performed computations of the free convective flow in a cubical enclosure in the presence of a magnetic field. Table 6 gives the values of the average Nusselt number obtained when the magnetic field is oriented in the x-direction, for two values of Ha (100 and 200). The difference between our results and those of Ozoe and Okada can be seen to be very small (less than 1.5%).

4.3. Structure and intensity of the flow for the three orientations of the magnetic field

The numerical results obtained for the vertically oriented magnetic field show the appearance of the Hartmann layers near the top and bottom walls (Fig. 7(a)). The velocity decreases exponentially in these layers. The profiles with maximum velocity are those in contact with the lateral walls ($Z = 0$ and $Z = 1$). The position of the peaks in these layers shifts towards the top and bottom walls as the Ha number is increased from 0 to 100. Also, in the core (between the Hartmann layers) the U profile varies linearly with Y and is symmetrical with respect to plane PH ($Y = 0.5$). This distribution is similar to that given by the analytic solution. The parallel layers (Fig. 7(b)) consist of similar profiles, with same value of the maximum velocity and a plateau extending from $X = 0.25$ to $X = 0.75$, where the fluid possesses a vertical component of velocity close to zero.

The effect of the magnetic field orientation and strength on the flow is illustrated in Fig. 7(c) for the x-directed field at a Rayleigh $Ra = 10^5$. The damping of the flow increases for growing Ha (increasing magnetic field strength).

The theoretical estimation of the maximum velocity can also be performed here, for validation purposes, by considering, for example in the case of a vertical field and electrically insulating walls ($Jz = \sigma UB$), equilibrium in the core region between electromagnetic forces and buoyancy forces, which gives $U_{\text{core}} \approx Ra/Ha^2$, and Hartmann layers of order Ha^{-1}. Numerical application gives, for $Ra = 10^5$ and $Ha = 100$, $U = 10$, which compares well with the magnitude shown in Fig. 7(a).

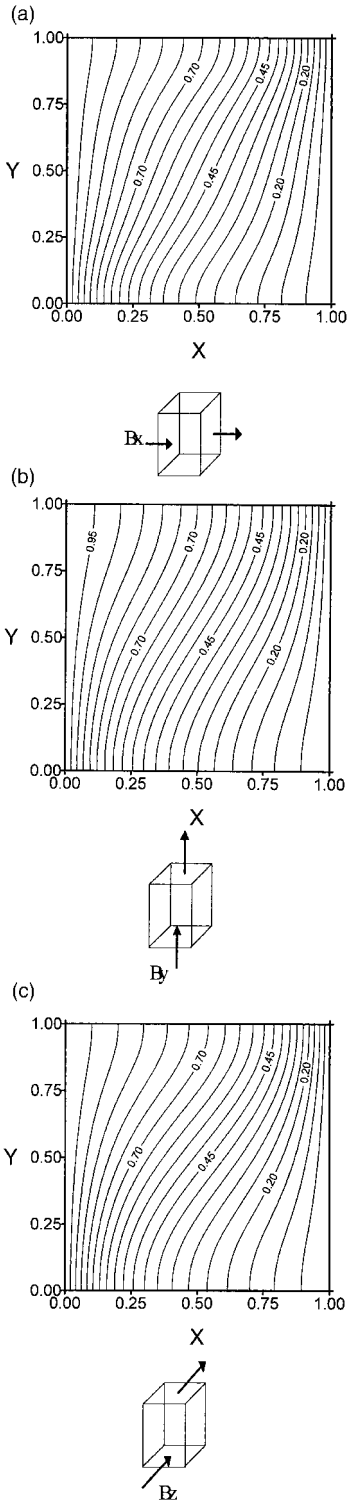

Fig. 9. Isotherms in plane PV for the three orientations of the magnetic field, when $Ha = 100$ and $Ra = 10^5$: (a) Bx; (b) By; (c) Bz.

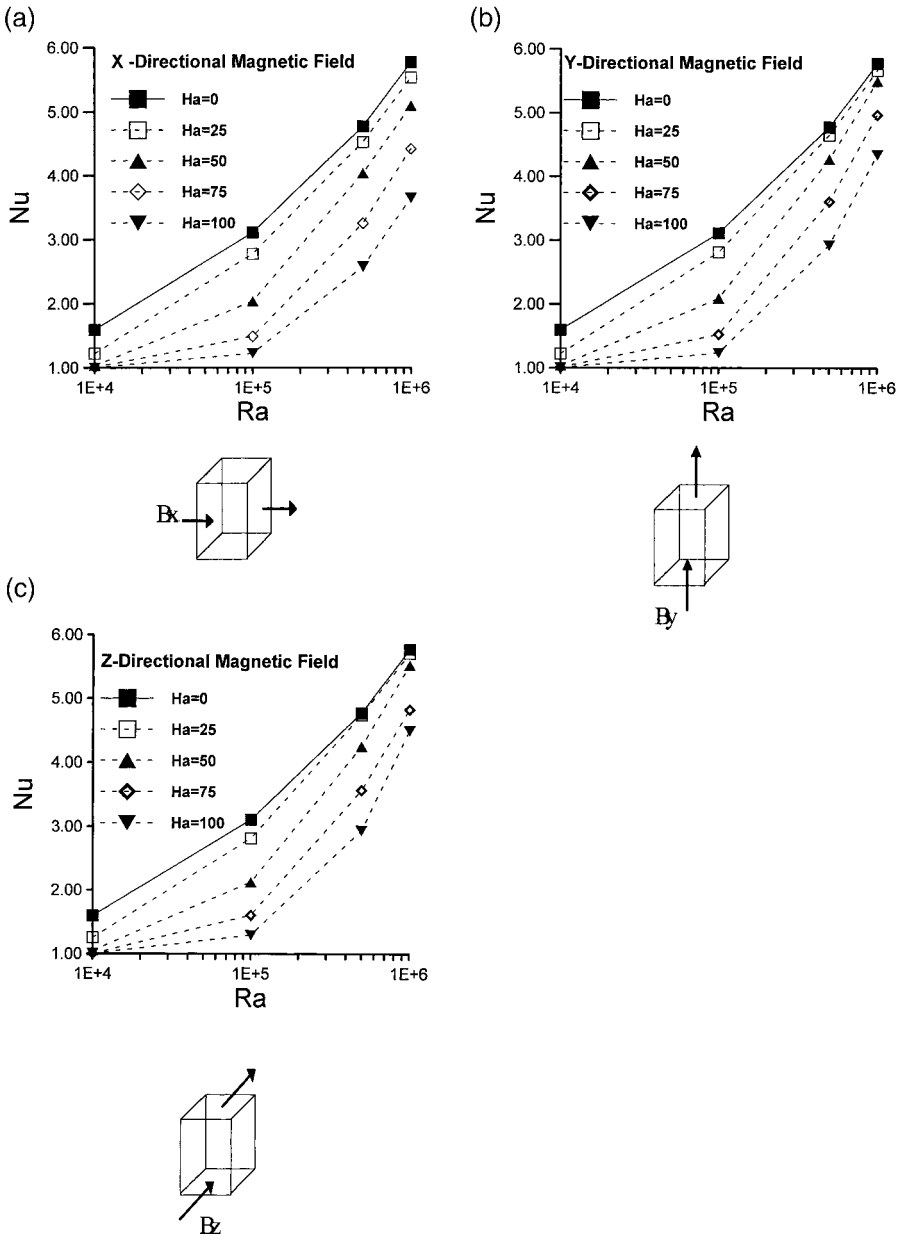

Fig. 10. Variation of the average Nusselt number as a function of *Ra, Ha* and magnetic field orientation: (a) *Bx*; (b) *By*; (c) *Bz*.

4.4. Current path and Lorentz force

For an *x*-oriented magnetic field, Fig. 7(d) shows the distribution of the vertical component *Fy* of the Lorentz force in plane PT. It acts as a sink term in the proximity of the hot wall and as a source term in the proximity of the cold wall. In both cases it counteracts the buoyancy force and leads to the reduction of the velocity of the various layers of the fluid. The current distribution responsible for this force is shown in Fig. 7(e) from which one can notice that negative currents are induced near the hot wall where the flow is directed upwards and positive currents induced near the cold wall where the flow is directed downwards and that due to wall electrical insulation the iso-current lines close within the fluid.

4.5. Effect on the thermal structure

The isotherms for the vertically directed magnetic

field are shown in Figs. 8(a)–(c). Strong convection is indicated by distorted isotherms within the cavity. As the *Ha* is increased, thermal stratification in the core is more and more destroyed and the isotherms become more and more parallel to the vertical walls, indicating the dominance of the conduction regime.

Also, the isotherms in the horizontally oriented magnetic field case (Fig. 9(a)) are the least distorted implying the reduced convective heat transfer as compared to other orientations.

4.6. Nusselt number variation

The above conclusions are further supported by Figs. 10(a)–(c) giving the variation of the Nusselt number as the Rayleigh and the Hartmann numbers are increased. As can be seen the damping is highest for values of *Ra* situated around the value $Ra = 10^5$ and for high strengths of the magnetic field.

4.7. Effect of wall conductivity

Figs. 11(a) and (b) show that for insulated walls the surface representing the distribution of electric potential presents variations less important than those corresponding to conducting walls. These high gradients in electric potential in the case of conducting walls are reflected, according to Ohm's law [Eq. (8)] in higher values of the electric current (Figs. 12(a) and (b)) and hence in those of the Lorentz force. Wall electrical conducting leads therefore to lower source or to higher sink terms in the momentum equations, depending on the flow direction; i.e. to an overall damping of the flow. This can be noticed through the comparison of the maximum velocities shown in Fig. 7(c). Another way for viewing the effect of magnetic field is to use the Lycoudis number *Ly* defined by $Ly = 2\ Ha^2/Ra^{1/2}$ and traditionally employed to correlate the heat transfer rate of free convection of a liquid metal in an external magnetic field (Lycoudis [18]; Okada and Ozoe [19]). The combination of the *Ha* and *Ra* in a single number has been dictated by the fact that damping is only limited to a certain range of the Rayleigh number (Figs. 13(a)–(c)). All three figures show that convection is best damped when the walls are electrically conducting.

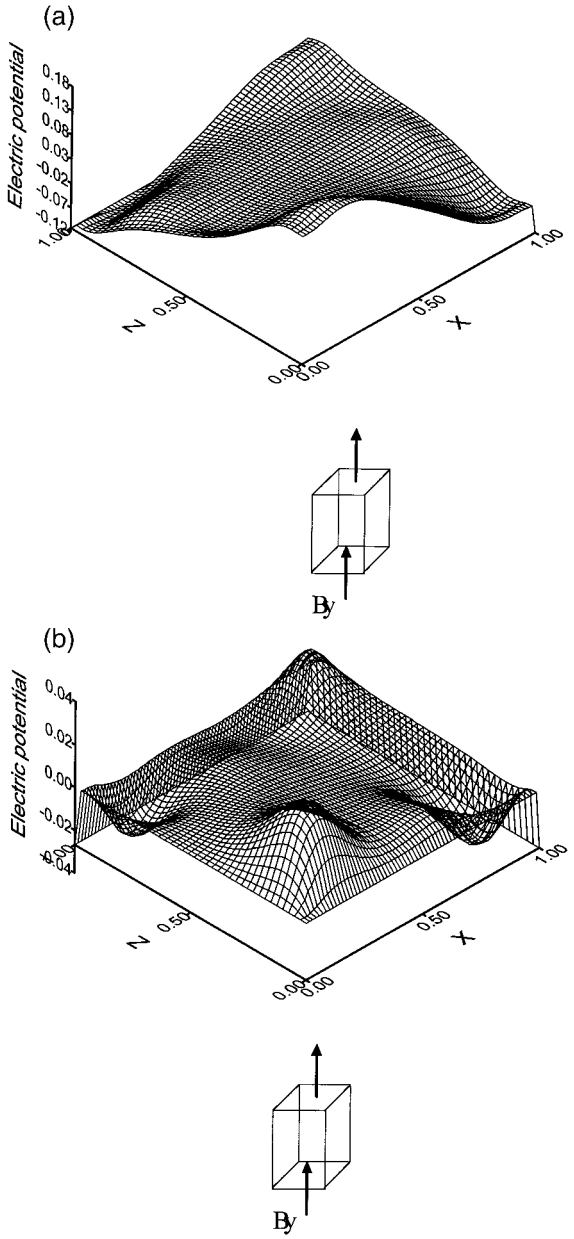

Fig. 11. Distribution of electrical potential in plane PH for $Ha = 75$ and $Ra = 10^5$: (a) insulating walls; (b) conducting walls.

5. Conclusion

A numerical procedure to predict the effect of wall electrical conductivity and magnetic field direction on natural-convective flow in a cavity has been proposed. A good concordance between numerical results and experimental or analytical data was obtained during code validation.

In the absence of a magnetic field the flow of gallium showed a behaviour which is different from that of an ordinary fluid and a heat transfer coefficient which is not uniform on the cold and hot faces of the cavity.

When a vertical magnetic field is imposed in a relatively shallow bi-dimensional cavity (of aspect ratio

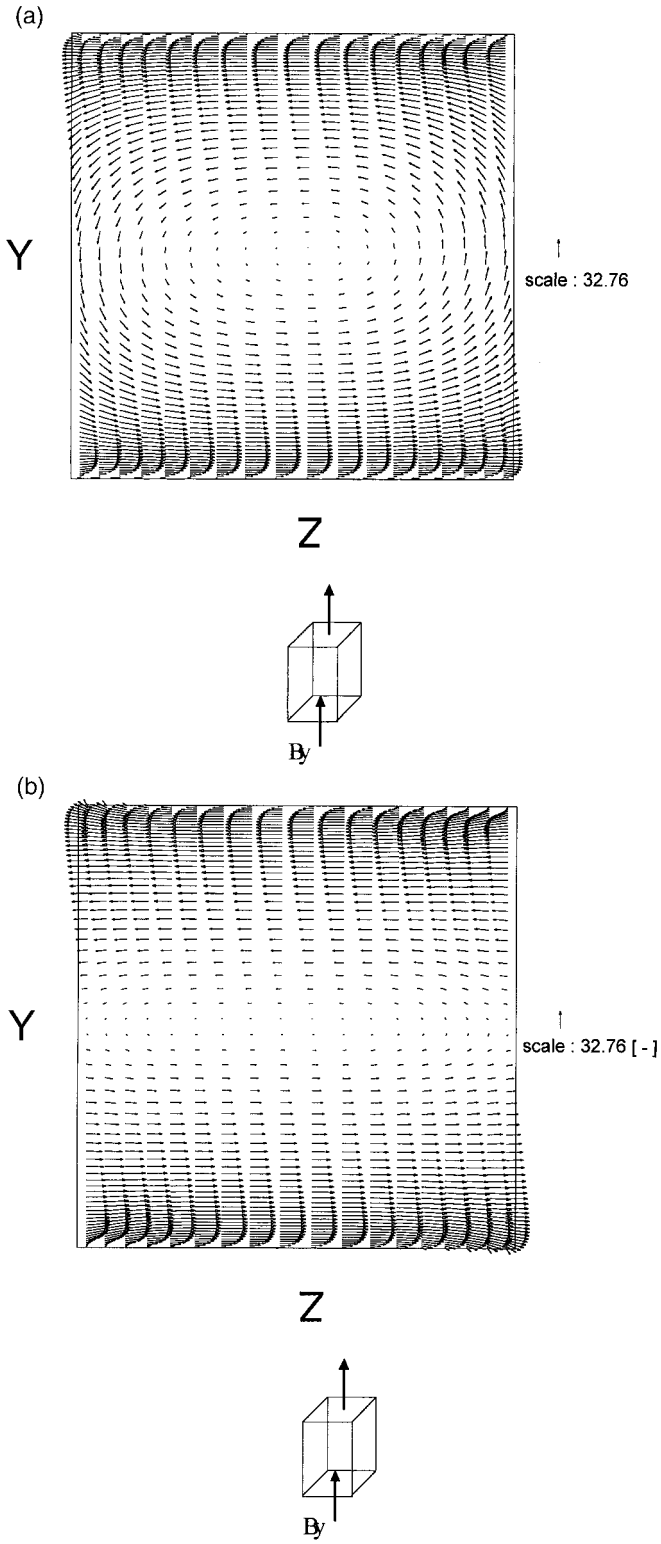

Fig. 12. Projection of electric current vectors in plane PT for $Ha = 75$ and $Ra = 10^5$: (a) insulating walls; (b) conducting walls.

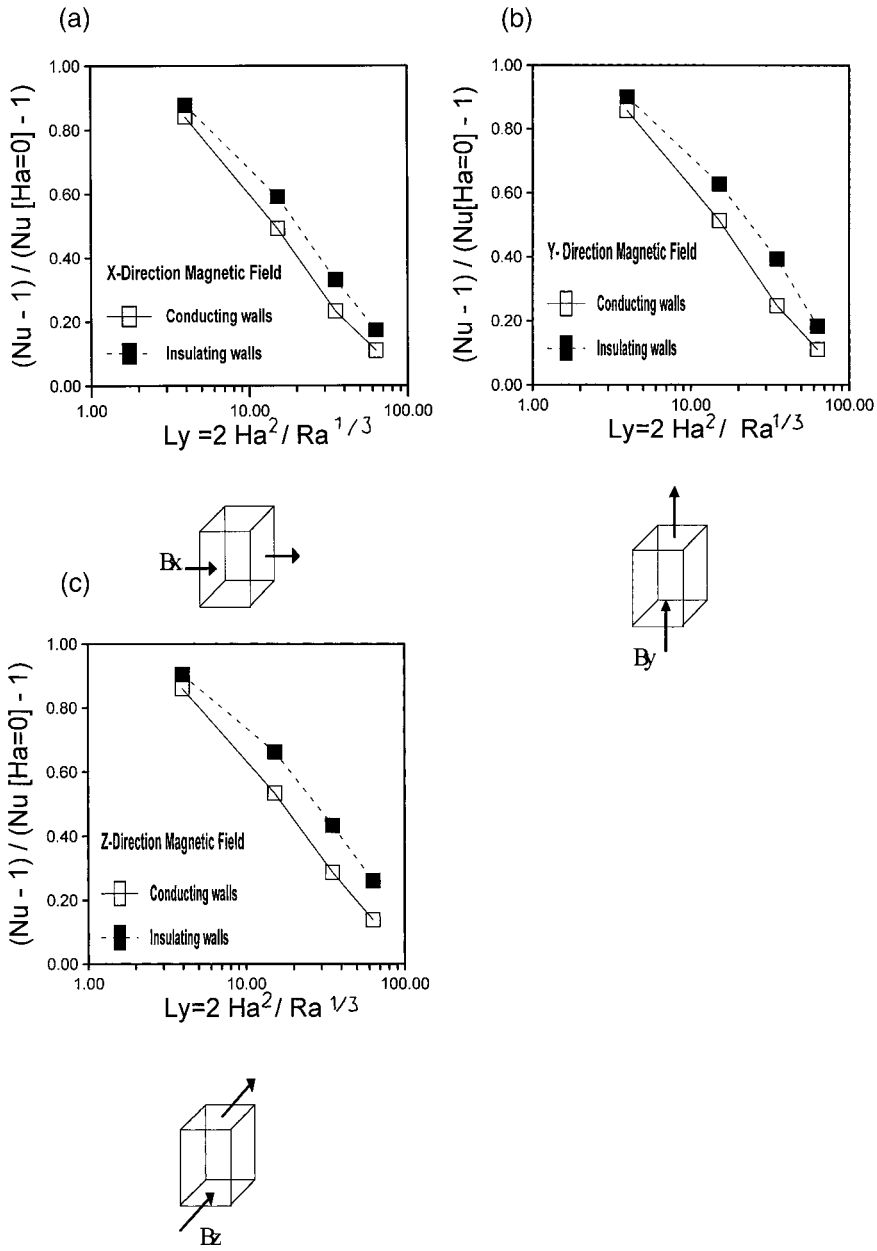

Fig. 13. Effect of wall electrical conductivity on heat transfer across the hot and cold faces: (a) *Bx*; (b) *By*; (c) *Bz*.

$A = 4$), the velocity profile changes from a cubic shape ($Ha = 0$) to one with a constant gradient throughout the core and peaks in the vicinity of the walls. The peaks shift towards the walls as Ha is increased.

The structure of the flow in the three-dimensional case is complex and showed Hartmann layers with varying value of the peaks in the z-direction. The side layers however have similar peaks. For a given orientation of the magnetic field, the maximum velocities in the cavity diminish as Ha is increased, implying a decrease in intensity of fluid currents circulating to-and-fro between the hot and cold walls. A comparison of the results for the three orientations revealed that the horizontal one leads to the best damping of the flow. Also, wall electrical conductivity changes the Lorentz force distribution by increasing it in regions where it opposes the flow and decreasing it in the remaining regions where it is favourable to the flow:

the consequence being an enhanced damping of the flow.

In conclusion, the results indicate that one can control the flow via a good choice of the strength and direction of the magnetic field, as well as of the electric conductivity of the cavity walls. In view of further studies aiming at investigating the utility of damping on the transport and fixation of dopants and impurities during crystal growth, the present numerical procedure appears to be a convenient tool which offers the possibility of a qualitative assessment of such a process.

References

[1] J.R. Carruthers, Crystal growth from the melt, in: N.B. Hannay (Ed.), Treatise on Solid State Chemistry, vol. 5, Plenum, New York, 1975, pp. 325–406.

[2] D.T.J. Hurle, Hydrodynamics in crystal growth, in: E. Kaldis, H.J. Scheel (Eds.), Crystal Growth and Materials, North-Holland, Amsterdam, 1977, pp. 550–569.

[3] N. Kobayashi, Heat transfer in Czochralski crystal growth, in: W.R. Wilcox (Ed.), Preparation and Properties of Solid State Materials, vol. 6, Basel/Marcel Dekker, New York, 1981, pp. 119–253.

[4] W.E. Langlois, Buoyancy-driven flows in crystal-growth melts, Annual Review Fluid Mechanics 17 (1985) 191–215.

[5] K. Hoshikawa, H. Hirata, H. Nakanishi, K. Ikuta, Control of oxygen concentration in CZ silicon growth, in: Proceedings of the 4th International Symposium on Silicon Matter Science Technology, Minneapolis, Electrochem. Soc., Princeton, NJ, 1981, pp. 101–112. Volume on Semiconductor Silicon.

[6] K.M. Kim, G.H. Schwuttke, P. Smetana, Apparatus for Czochralski silicon crystal growth through axial magnetic field fluid damping, IBM Tech. Duscl. Bu 24 (1981) 3376–3377.

[7] T.A. Campbell, J.N. Koster, Radioscopic visualization of indium antimonide growth by the vertical Bridgman–Stockbarger technique, Journal of Crystal Growth 147 (1995) 408–410.

[8] L. Davoust, F. Bertrand, R. Moreau, P.A. Tanguy, R. Bolcato, Recent results on MHD damped convection in the horizontal Bridgman configuration, The 14th International Riga Conference of Magnetohydrodynamics, Jurmala, Latvia, 1995.

[9] H. Benhadid, D. Henry, Numerical simulation of convective three-dimensional flows in a horizontal cylinder under the action of a constant magnetic field, Journal of Crystal Growth 166 (1996) 436–445.

[10] S. Alchaar, P. Vasseur, E. Bilgen, Natural convection heat transfer in a rectangular enclosure with a transverse magnetic field, Journal of Heat Transfer 117 (1995) 669–673.

[11] L. Bühler, Magneto-convection in long vertical channels, in: Proceedings of the Aussois Conference of MHD Flows, Aussois, France, 1997, pp. 391–396.

[12] J.P. Garandet, T. Alboussière, R. Moreau, Buoyancy driven convection in a rectangular enclosure with a transverse magnetic field, Int. J. Heat Mass Transfer 35 (4) (1992) 741–748.

[13] S.V. Patankar, Numerical Heat Transfer and Fluid Flow, McGraw-Hill, New York, 1980.

[14] Davis G. De Vahl, Natural convection of air in a square cavity: a bench mark numerical solution, International Journal for Numerical Methods in Fluids 3 (1983) 249–264.

[15] F. Wolff, C. Beckermann, R. Viskanta, Natural convection of liquid metals in vertical cavities, Experimental Thermal and Fluid Science 1 (1988) 83–91.

[16] Davis G. De Vahl, J.P. Jones, Natural convection in a square cavity: a comparison exercise, International Journal for Numerical Methods in Fluids 3 (1983) 227–248.

[17] H. Ozoe, K. Okada, The effect of the direction of the external magnetic field on the three-dimensional natural convection in a cubical enclosure, Int. J. Heat Mass Transfer 32 (10) (1989) 1939–1954.

[18] P.S. Lycoudis, Natural convection of an electrically conducting fluid in the presence of a magnetic field, Int. J. Heat Mass Transfer 5 (1962) 23–34.

[19] K. Okada, H. Ozoe, Experimental heat transfer rates of natural convection of molten gallium suppressed under an external magnetic field in either the x-, y- or z-direction, Journal of Heat Transfer 114 (1992) 107–114.